TITLE

Mutations in the β-tubulin TUBB impair ciliogenesis and are associated with ciliopathy-like phenotypes

AUTHORS

Antonio Mollica[1,2], Safia Omer[3], Georgiana Forguson[1], Sydney Steiman[1,4], Sonia L. Evagelou[1], Serhiy Naumenko[5], Susan Walker[6], Lu Yi Li[1], Aideen Teeling[1], Kyle Lindsay[1], Steven Erwood[1,7], Shagana Visuvanathan[1], Anjali Vig[1], Robert M. Vernon[8], Benjamin Akman[9], Constance Smith-Hicks[9,10], Julie D. Forman-Kay[2,8], Manohar Shroff[11,12], Vivek Pai[11,12], Rene E. Harrison[3], Ronald D. Cohn[1,7,13], Evgueni A. Ivakine[1,4,7,*]

AFFILIATIONS

[1] Genetics and Genome Biology Program, The Hospital for Sick Children, Toronto, ON, Canada.

[2] Department of Biochemistry, University of Toronto, Toronto, ON, Canada.

[3] Department of Biological Sciences, University of Toronto Scarborough, Toronto, ON, Canada.

[4] Department of Physiology, University of Toronto, Toronto, ON, Canada.

[5] Department of Biostatistics, Harvard Chan School of Public Health, Boston, MA, USA.

[6] The Centre for Applied Genomics, The Hospital for Sick Children, Toronto, ON, Canada.

[7] Department of Molecular Genetics, University of Toronto, Toronto, ON, Canada.

[8] Molecular Medicine Program, The Hospital for Sick Children, Toronto, ON, Canada.

[9] Department of Neurology and Developmental Medicine, Kennedy Krieger Institute, Baltimore, MD, USA.

[10] Department of Neurology, Johns Hopkins University School of Medicine, Baltimore, MD, USA.

[11] Division of Neuroradiology, Department of Diagnostic and Interventional Radiology, The Hospital for Sick Children, Toronto, ON, Canada.

[12] Department of Medical Imaging, University of Toronto, Toronto, ON, Canada.

[13] Department of Pediatrics, The Hospital for Sick Children, Toronto, ON, Canada.

*Corresponding author: zhenya.ivakine@sickkids.ca

SUPPLEMENTARY FIGURES

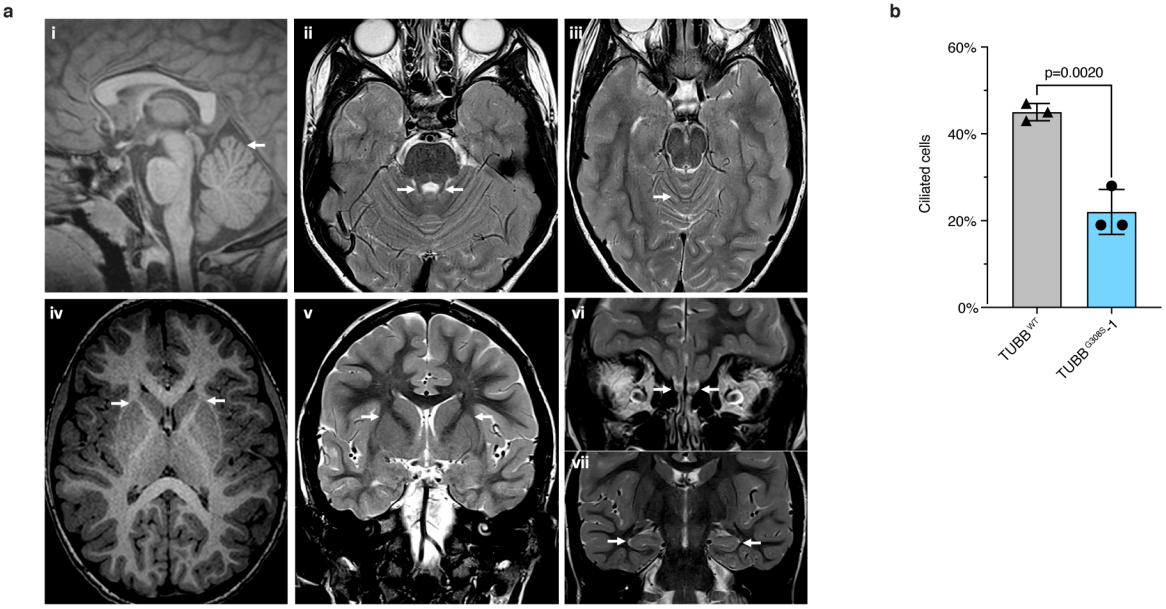
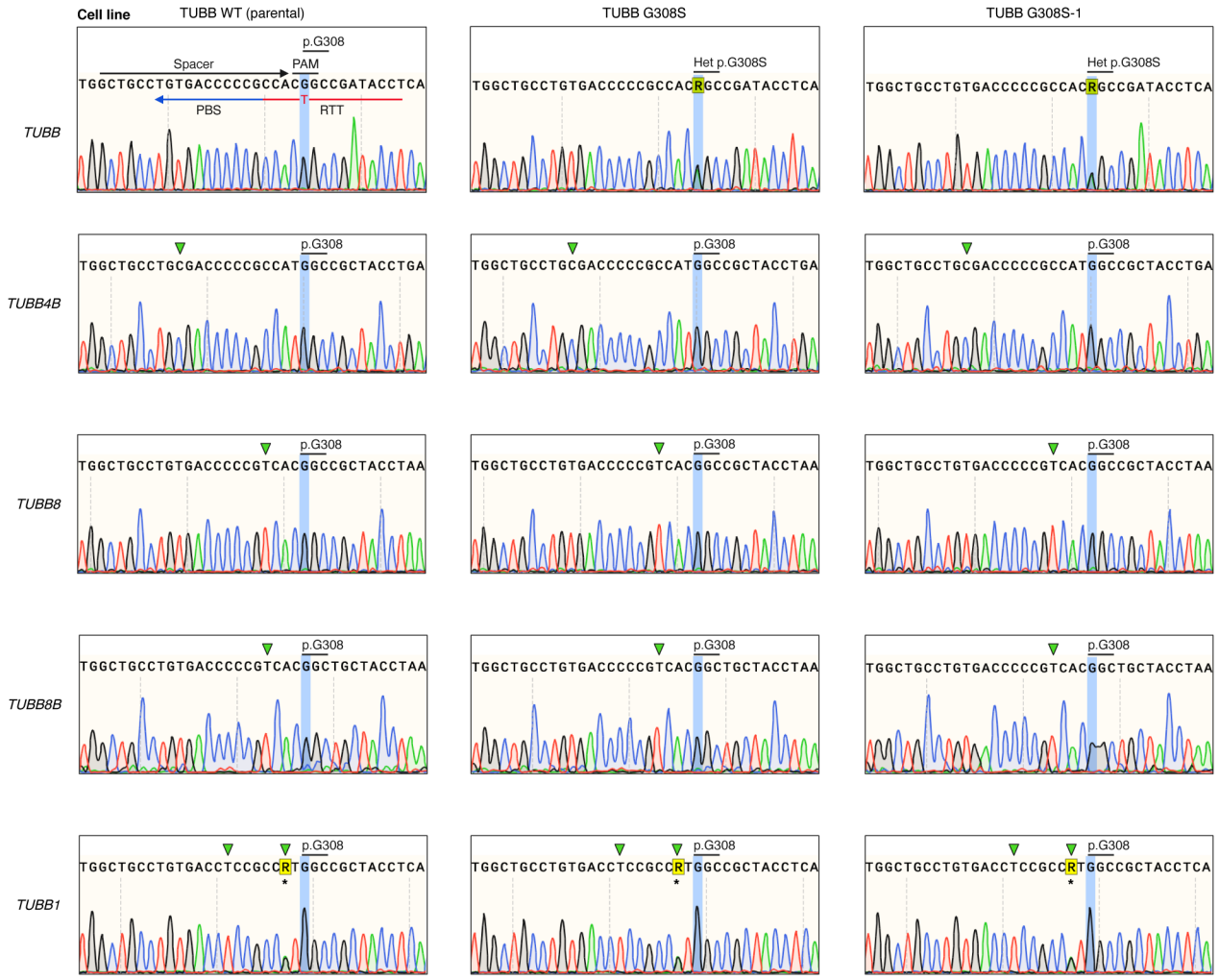


Figure S1. Heterozygous TUBB^{G308S} hTERT-RPE1 cells show reduced ciliation. (a) Magnetic resonance imaging (MRI) of the brain of a healthy control subject. [i] Sagittal 3D T1 image demonstrates normal morphology of the superior vermis (white arrow). [ii, iii] Axial T2 images show normal appearances of the superior cerebellar peduncles (white arrows in ii) and the superior vermis (white arrow in iii). [iv, v] Axial reformat of the 3D T1 sequence [iv] and coronal T2 [v] show normal symmetric appearances of the basal ganglia (white arrows). [vi] Coronal T2 image shows normal symmetric appearances of the olfactory tracts (white arrows). [vii] Coronal T2 image shows normal appearances of the hippocampal formations with preserved internal architecture (white arrows). (b) Percentage of cells showing ARL13B-positive cilium in TUBB^{WT} and TUBB^{G308S}-1 cells (TUBB^{G308S} clone 1) after 48 h serum withdrawal. Data from three experiments ($n \geq 199$ per cell line per experiment) are represented as mean $\pm$ standard deviation. P-value was calculated using an unpaired two-tailed t-test.

Source data are provided as a Source Data file.



* Known heterozygous single nucleotide polymorphism in hTERT RPE-1 (ATCC CRL-4000) cells [NCBI Short Read Archive (SRA)-Experiment ID: SRX858057]

Figure S2. Heterozygous TUBB^{G308S} hTERT-RPE1 cells are not edited at the most likely off-target sites. Sanger sequencing electropherograms of the target site (*TUBB* locus; upper panel) and the four most likely predicted protein-coding off-target sites (*TUBB4B, TUBB8, TUBB8B, TUBB1* loci; lower panels) in the generated heterozygous TUBB^{G308S} cell models and parental TUBB^{WT} cells. The target base in the *TUBB* locus and the corresponding base in the off-target loci are highlighted in blue. The analyzed off-target sites correspond to protein-coding regions of the human genome showing single or double mismatches with the spacer sequence of the used prime editing guide RNA (pegRNA). Green triangles indicate mismatch sites. PAM: protospacer adjacent motif; PBS: primer binding site; RTT: reverse transcriptase template.

Created in BioRender. Forguson, G. (2025) https://BioRender.com/u0svhxw

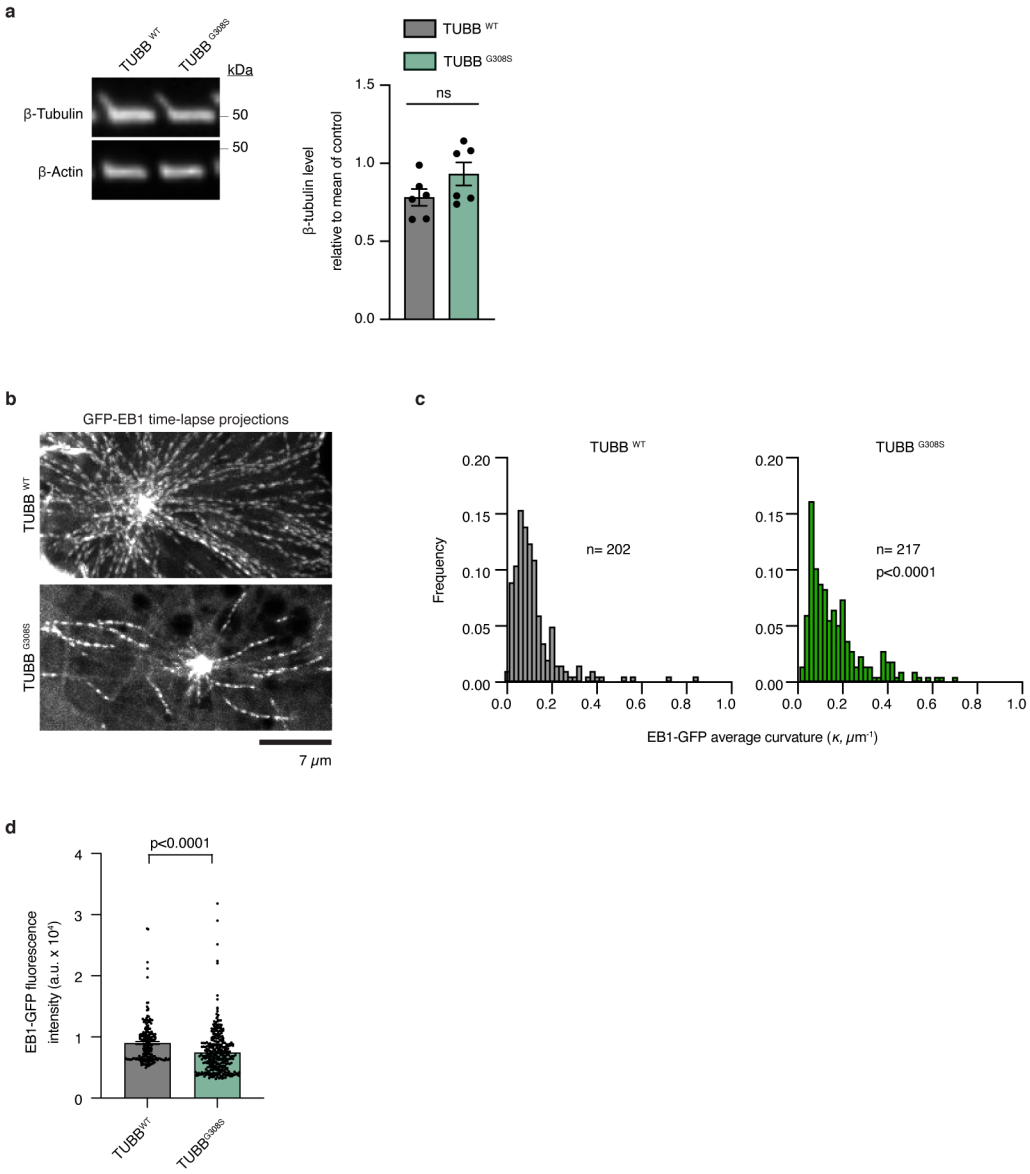


Figure S3. Heterozygous TUBB^{G308S} hTERT-RPE1 cells nucleate fewer microtubules that show excessive curvature. (a) Representative immunoblot of total cell lysates from TUBB^{WT} and TUBB^{G308S} hTERT-RPE1 cells (n = 6 per cell line) probed for β-tubulin and the loading control β-actin. Bar graph shows β-tubulin signal intensity normalized to β-actin and plotted relatively to the mean of TUBB^{WT} cells. Data from six experiments are represented as mean ± standard error of the mean. P-value was calculated using an unpaired two-tailed t-test. ns = not statistically significant ($p > 0.05$). (b) Representative spinning disk confocal images of TUBB^{WT} and TUBB^{G308S} cells expressing EB1-GFP. EB1-GFP projections were generated from maximum intensity projection of 12 frames captured with 4 seconds intervals. Growing microtubule ends appear as bright tracks. (c) Histogram of the frequency of the average curvature of EB1-GFP projections in TUBB^{WT} (n = 202 EB1-GFP projections) and TUBB^{G308S} (n = 217 EB1-GFP projections) cells. Data

are from three experiments. P-value was calculated using a two-tailed Mann U Whitney test. (d) Scatter plot of the mean fluorescence intensity of EB1-GFP comets in transiently transfected $TUBB^{WT}$ and $TUBB^{G308S}$ cells (n = 215 comets for $TUBB^{WT}$ cells and n = 335 comets for $TUBB^{G308S}$ cells, from three experiments). Data are represented as mean ± standard error of the mean. P-value was calculated using an unpaired two-tailed t-test.

Source data are provided as a Source Data file.

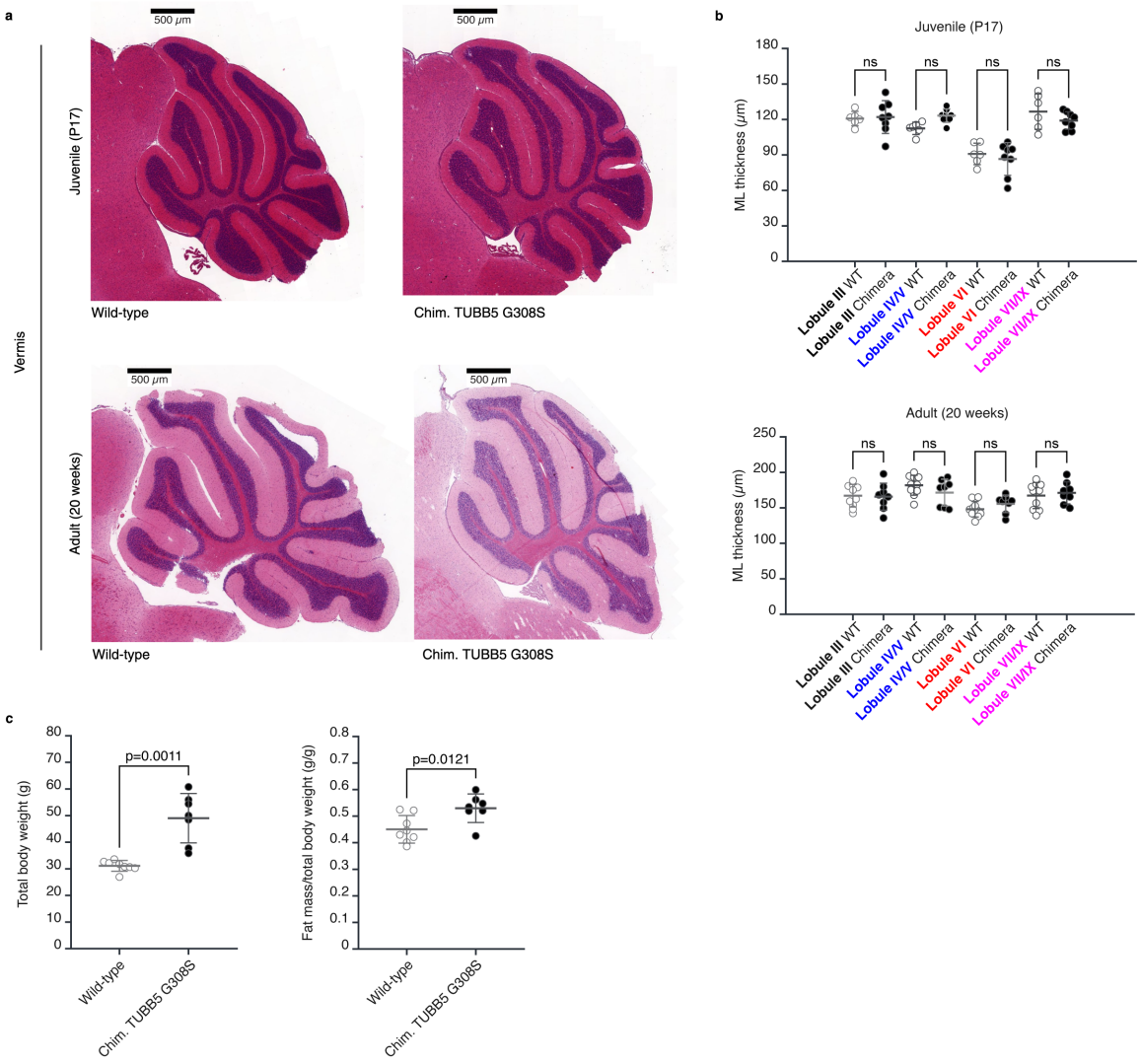


Figure S4. TUBB5 G308S chimeric mice show normal cerebellum morphology and increased visceral fat. (a) Representative hematoxylin and eosin (H&E) staining of cerebellar sections from wild-type and TUBB5 G308S chimeric mice at postnatal day 17 (P17, juvenile) and 20 weeks of age (adult). (b) Quantification of molecular layer (ML) thickness across cerebellar lobules III, IV/V, VI, and VII/IX in wild-type and TUBB5 G308S chimeric mice at P17 and 20 weeks of age. Each data point represents one measurement; two points within one field of view were measured per animal (P17: n = 3 wild-type mice, n = 4 TUBB5 G308S chimeric mice; adult: n = 5 wild-type mice, n = 4 TUBB5 G308S chimeric mice). P-values were calculated using one-way ANOVA followed by Tukey's multiple comparisons test. (c) Total body weight (left graph) and body fat composition (fat mass/total body weight; right graph) of adult wild-type and TUBB5 G308S chimeric mice measured using dual-energy X-ray absorptiometry (DEXA) (n = 8 wild-type, n = 7 TUBB5 G308S chimeric mice). P-values were calculated using an unpaired two-tailed t-test with Welch's correction (total body weight) and an unpaired two-tailed t-test (body fat composition).

Data are represented as mean ± standard deviation. ns = not statistically significant ($p > 0.05$).

Created in BioRender. Forguson, G. (2025) https://BioRender.com/u0svhxw. Source data are provided as a Source Data file.

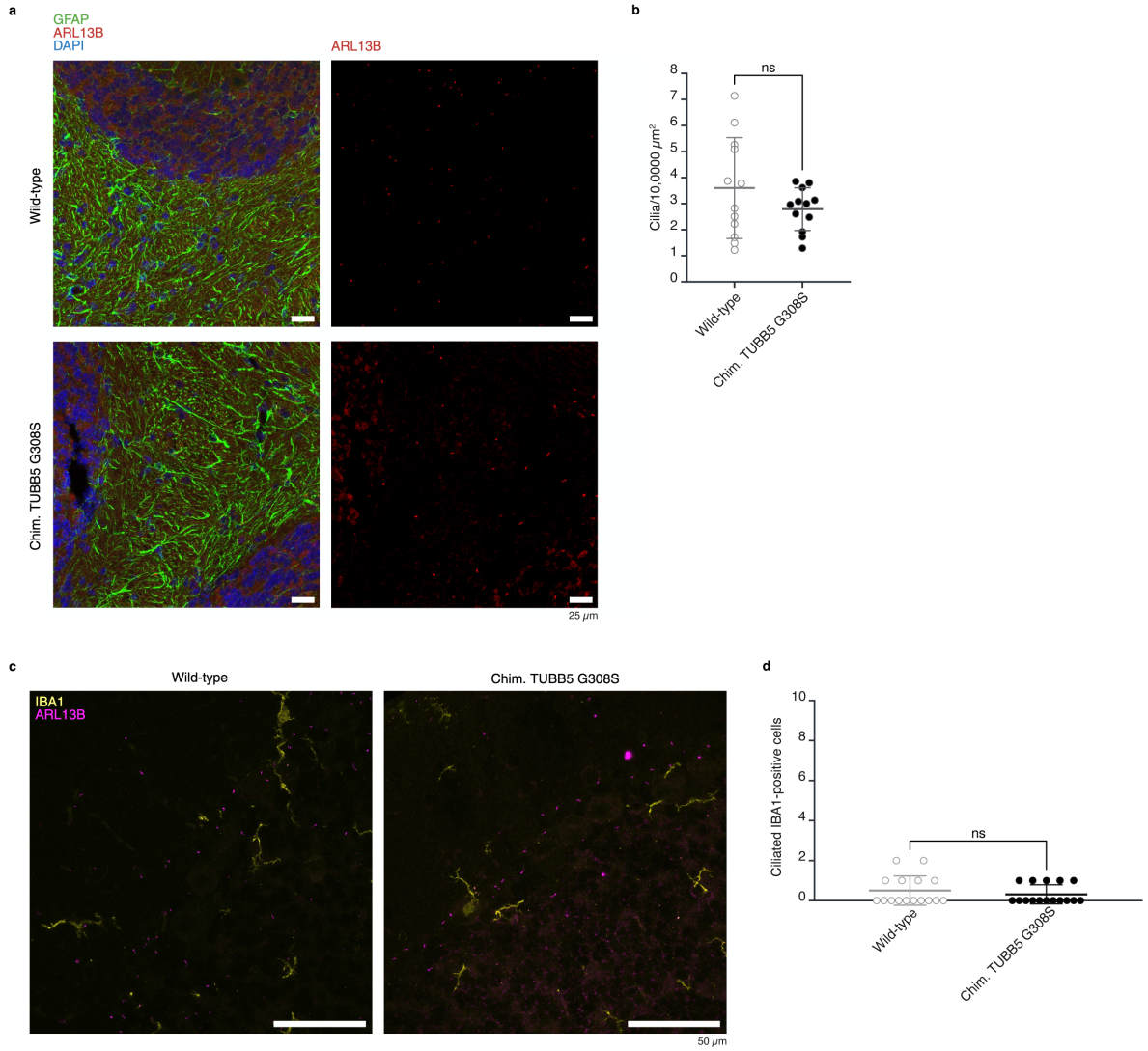


Figure S5. TUBB5 G308S chimeric mice show normal ciliation in the cerebellar white matter and microglia. (a) Representative images of the cerebellar white matter region from adult wild-type and TUBB5 G308S chimeric mice immunostained for the ciliary marker ARL13B (red), the astrocyte marker GFAP (green), and counterstained with DAPI (blue). (b) Quantification of ARL13B-positive cilia within the cerebellar white matter region of adult mice, as demarcated by GFAP-positive astrocytes. Each data point represents one field of view; three fields of view were scored per animal (n = 4 wild-type mice, n = 4 TUBB5 G308S chimeric mice). P-value was calculated using an unpaired two-tailed t-test. (c) Representative images of cerebellar lobules I/II from adult wild-type and TUBB5 G308S chimeric mice immunostained for the ciliary marker ARL13B (magenta) and the microglia marker IBA1 (yellow). (d) Quantification of cerebellar IBA1-positive microglia cells bearing ARL13B-positive cilia in adult wild-type and TUBB5 G308S chimeric mice. Ciliated cells were scored within each field of view (291^2 μm²). Each data point represents

one field of view; four fields of view were scored per animal (n = 4 wild-type mice, n = 4 TUBB5 G308S chimeric mice). P-values were calculated using a two-tailed Mann U Whitney test.

Data are represented as mean ± standard deviation. ns = not statistically significant ($p > 0.05$).

Created in BioRender. Forguson, G. (2025) https://BioRender.com/u0svhxw. Source data are provided as a Source Data file.

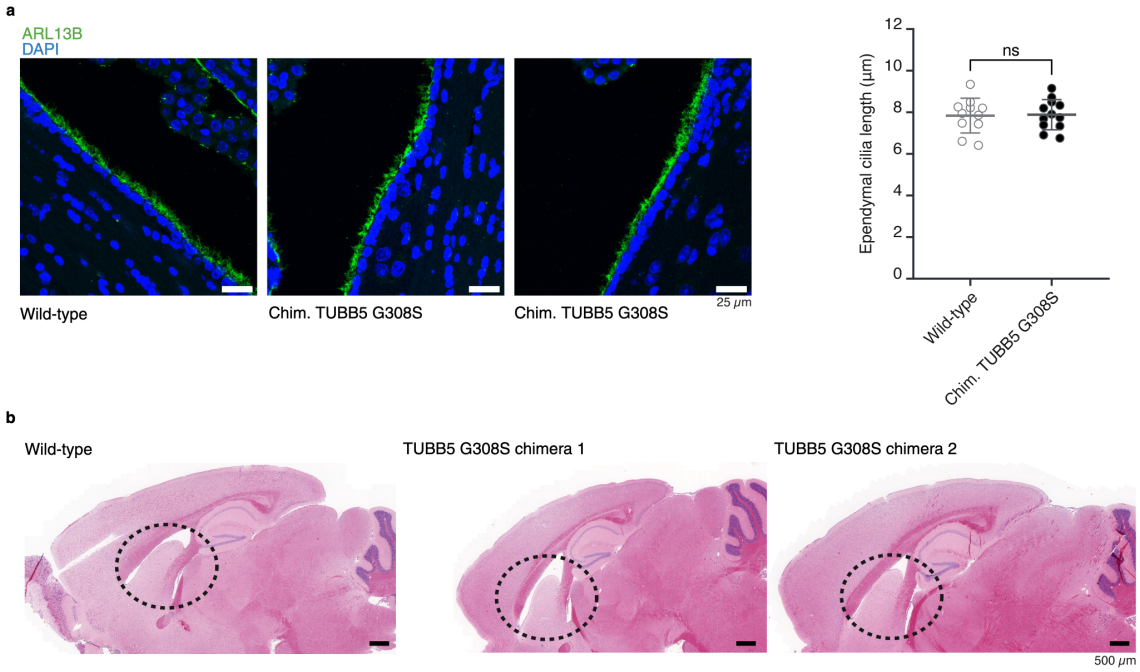


Figure S6. TUBB5 G308S chimeric mice show normal motile ependymal cilia. (a) Representative images of ciliated ependymal cells lining the third ventricle from adult wild-type and TUBB5 G308S chimeric mice immunostained for the ciliary marker ARL13B (green) and counterstained with DAPI (blue), showing no overt differences in motile cilia morphology. Images for TUBB5 G308S chimeric mice are from two different animals; similar results were observed in all 4 TUBB5 G308S chimeric mice and 4 wild-type mice analyzed. Scatter plot shows the length of ARL13B-positive cilia lining the third ventricle. Each data point represents the average cilia length from three measurement points per field of view; at least two fields of view were scored per animal (n = 4 wild-type mice, n = 4 TUBB5 G308S chimeric mice). Data are represented as mean ± standard deviation. P-value was calculated using an unpaired two-tailed t-test. (b) Representative hematoxylin and eosin (H&E)-stained sagittal brain sections from adult wild-type and TUBB5 G308S chimeric mice. The ventricles are indicated by dashed circles. Similar results were observed in all 4 TUBB5 G308S chimeric mice and 4 wild-type mice analyzed.

Created in BioRender. Forguson, G. (2025) https://BioRender.com/u0svhxw. Source data are provided as a Source Data file.

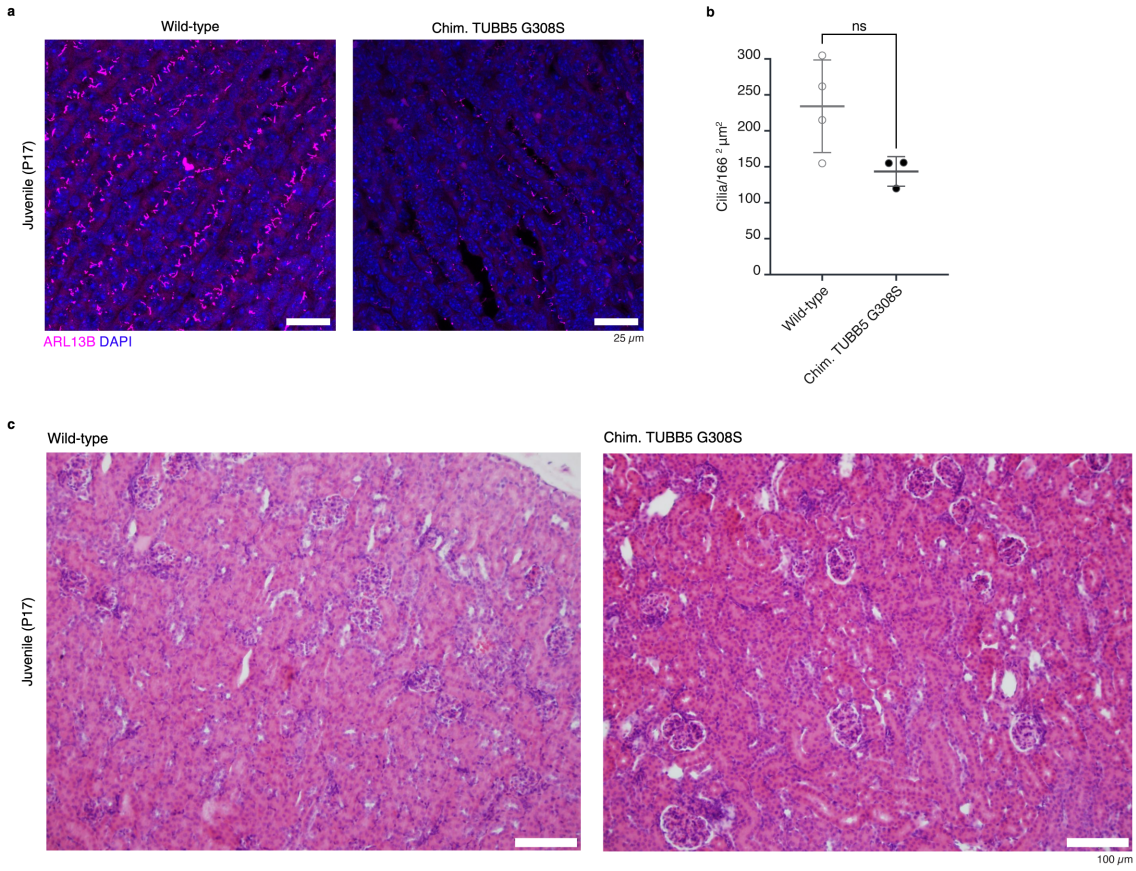
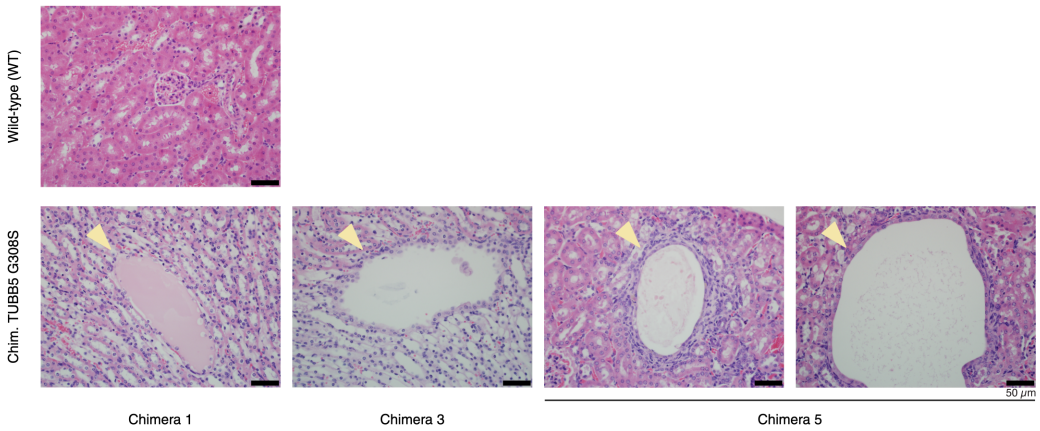


Figure S7. Juvenile TUBB5 G308S chimeric mice show a non-significant trend towards reduced kidney ciliation without histological abnormalities. (a) Representative images of kidney sections from juvenile (P17) wild-type and TUBB5 G308S chimeric mice immunostained for the ciliary marker ARL13B (magenta) and counterstained with DAPI (blue). (b) Quantification of ARL13B-positive kidney cilia in tubular epithelial cells of P17 wild-type and TUBB5 G308S chimeric mice. Each data point represents an average per animal; four fields of view were scored per animal (n = 4 wild-type mice, n = 3 TUBB5 G308S chimeric mice). Data are represented as mean ± standard deviation. P-value was calculated using an unpaired two-tailed t-test. (c) Representative images of hematoxylin and eosin (H&E) staining of kidney sections from P17 wild-type and TUBB5 G308S chimeric mice showing normal histology and absence of cystic lesions.

Created in BioRender. Forguson, G. (2025) https://BioRender.com/u0svhxw. Source data are provided as a Source Data file.

a



b

Sample ID	Kidney area (µm^2)	Number of cysts	Total cystic area (µm^2)	% cystic area
WT	39614695.48	0	0	0
Chimera 1	62658690.29	1	17323.14	0.027646827
Chimera 2	57556768.96	0	0	0
Chimera 3	57085735.76	1	32377.78	0.056717811
Chimera 4	36508938.71	0	0	0
Chimera 5	54173366.23	2	92251.91	0.170290156

Figure S8. Quantification of tubular cystic area in adult TUBB5 G308S chimeric mice. (a) Hematoxylin and eosin (H&E) staining of kidney sections from adult wild-type (WT) and TUBB5 G308S chimeric mice, also shown in Figure 7c. This panel displays a representative image from wild-type tissue, alongside all observed cystic dilatations of tubules in chimeric mice (yellow arrowheads). (b) Quantification of the number of tubular cysts and tubular cystic area in adult TUBB5 G308S chimeric mice. Cystic area is also expressed as the percentage of total kidney area (cystic index).

Created in BioRender. Forguson, G. (2025) https://BioRender.com/u0svhxw

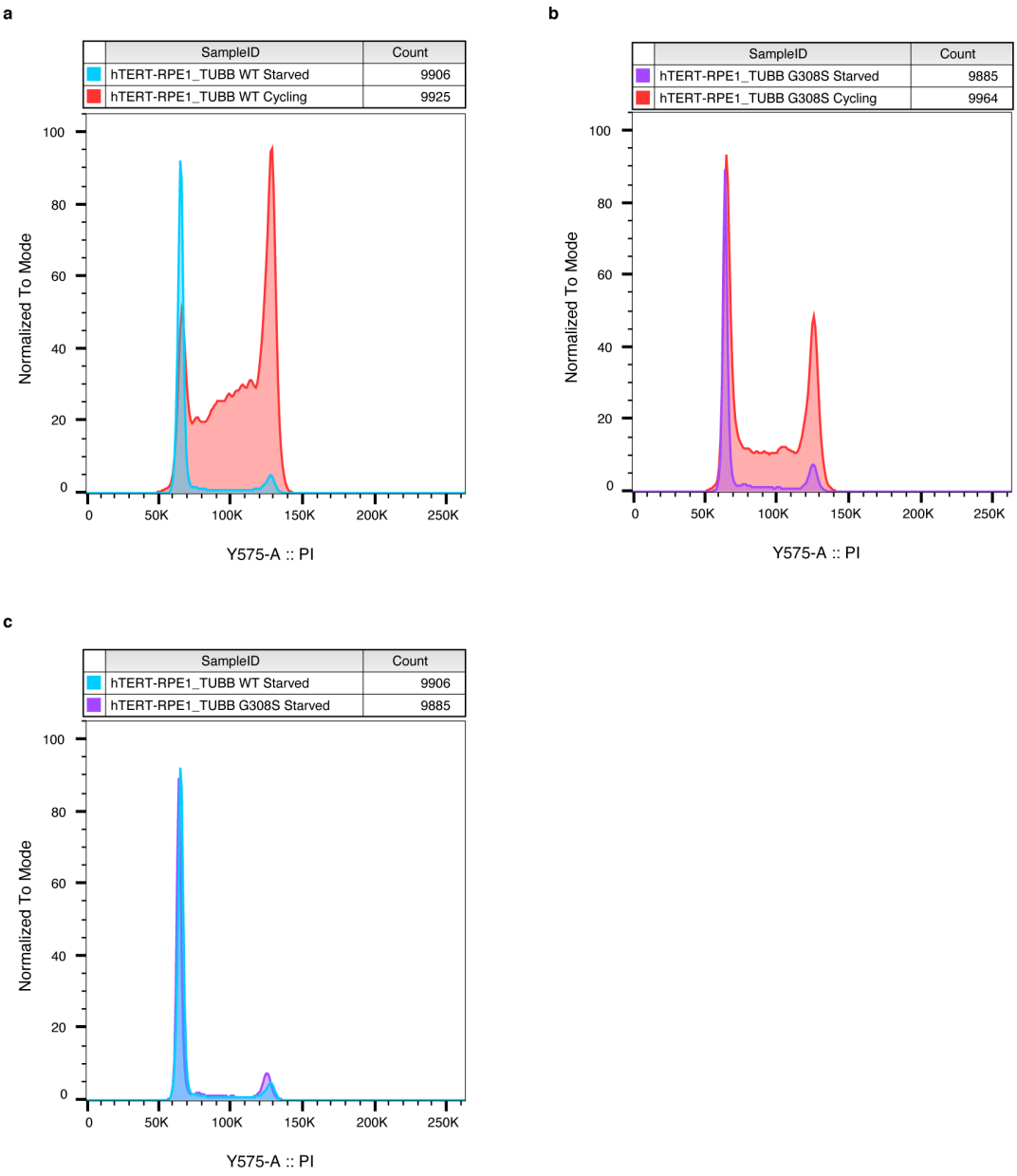


Figure S9. Heterozygous TUBB^{G308S} cells exit the cell cycle as effectively as TUBB^{WT} cells upon serum withdrawal. Cell cycle profiles of TUBB^{WT} and TUBB^{G308S} hTERT-RPE1 cells, cycling or after 48 h serum withdrawal to induce quiescence, obtained by flow cytometry analysis using propidium iodide (PI) as a stoichiometric DNA binding dye to measure DNA content. Data are represented as histograms of PI fluorescence intensity, normalized to mode to account for differences in cell number across the samples. (a) Overlaid histograms of cycling (red) and serum-starved (blue) TUBB^{WT} cells. (b) Overlaid histograms of cycling (red) and serum-starved (purple) TUBB^{G308S} cells. (c) Overlaid histograms of serum-starved TUBB^{WT} cells (blue) and serum-starved TUBB^{G308S} cells (purple).

Source data are provided as a Source Data file. This experiment was performed once.

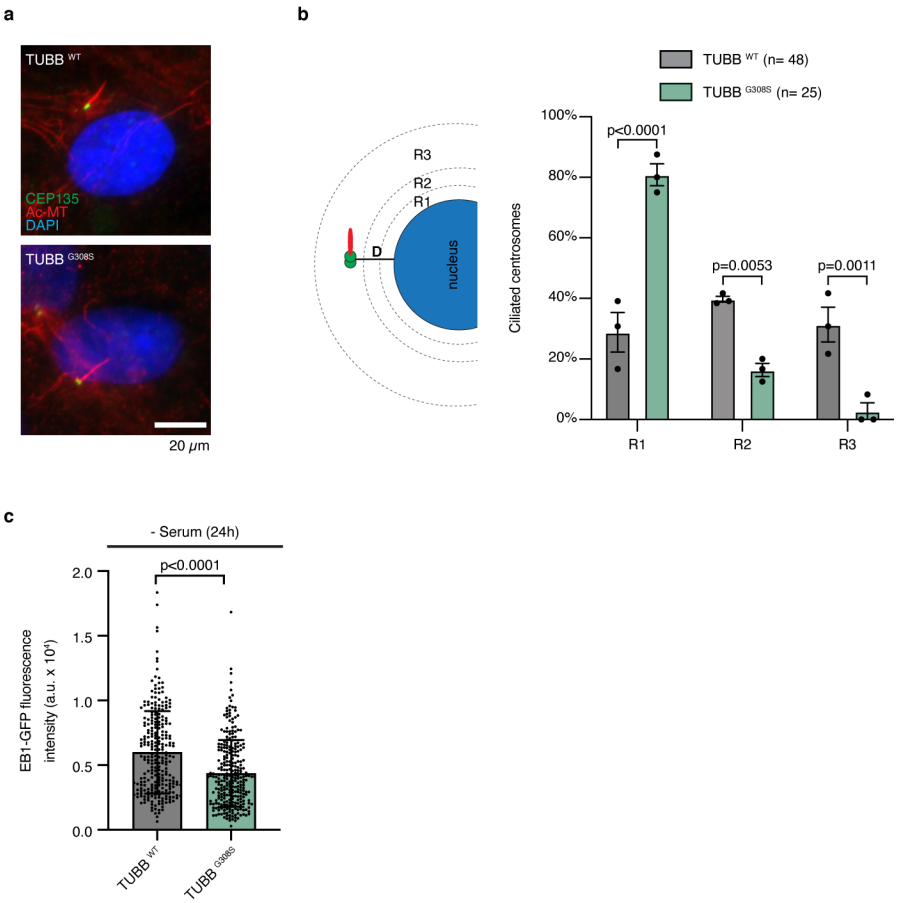


Figure S10. Heterozygous TUBB^{G308S} hTERT-RPE1 cells show defective primary cilia migration. (a) Representative images of ciliated TUBB^{WT} and TUBB^{G308S} cells fixed after 24 h serum withdrawal and immunostained for the centrosomal marker CEP135 (green), acetylated-α-tubulin (red) and DNA (blue) to label the nucleus. (b) Schematic representation showing the area around the nucleus of a ciliated cell. Distance (D) was measured between ciliated CEP135-positive centrosomes and the nearest margin of the nucleus. The following radii (R) were considered, from the nearest margin of the nucleus: R1 < 1 µm; 1 µm < R2 < 2 µm; R3 > 2 µm. Bar graph of the percentage of ciliated centrosomes observed within each designated region in TUBB^{WT} and TUBB^{G308S} cells after 24 h serum withdrawal. Data from three experiments (n = 48 ciliated TUBB^{WT} cells and n = 25 ciliated TUBB^{G308S} cells) are represented as mean ± standard error of the mean. P-value was calculated using two-way ANOVA followed by Šídák's multiple comparisons test. (c) Scatter plot of the mean fluorescence intensity of EB1-GFP comets in transiently transfected TUBB^{WT} and TUBB^{G308S} cells after 24 h serum withdrawal (n = 262 comets for TUBB^{WT} cells and n = 280 comets for TUBB^{G308S} cells, from three experiments). Data are represented as mean ± standard error of the mean. P-value was calculated using a two-tailed Mann U Whitney test.

Source data are provided as a Source Data file.

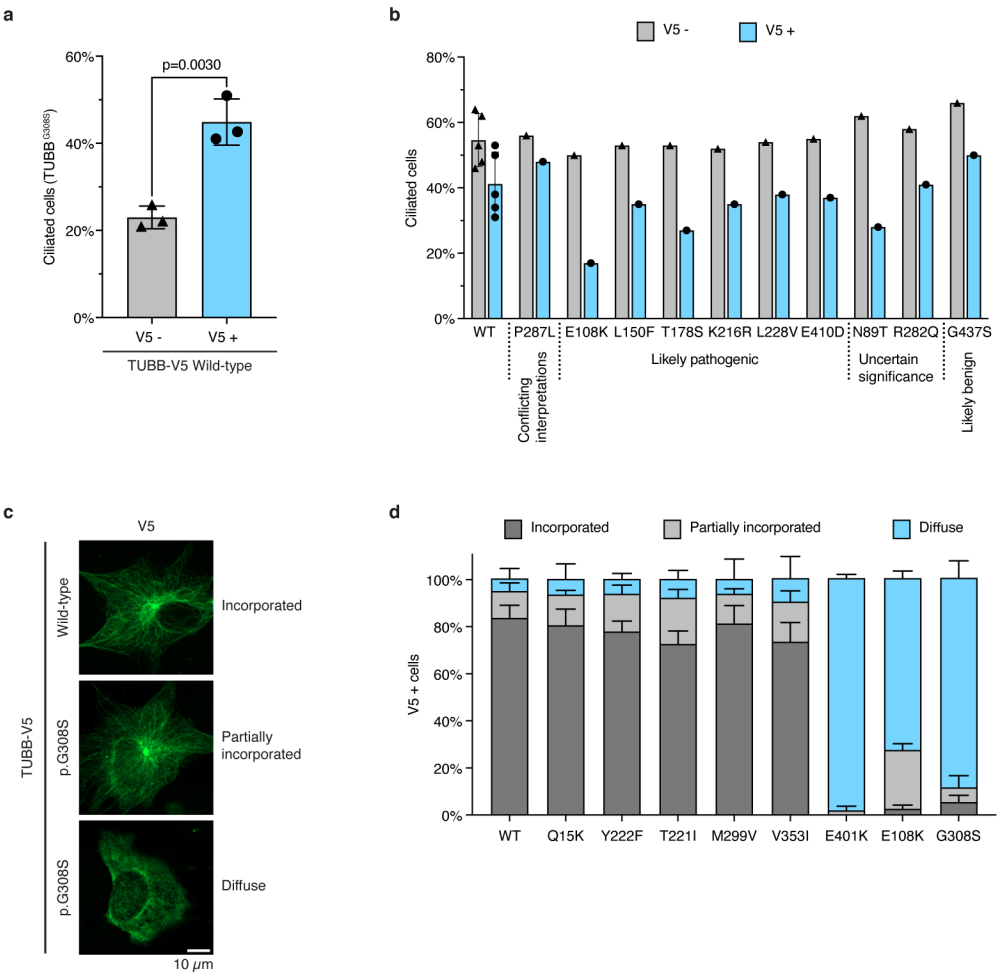


Figure S11. A subset of clinically relevant dominant mutations in TUBB affects ciliation and shows reduced incorporation into microtubules in hTERT-RPE1 cells. (a) Ciliation frequency of $TUBB^{G308S}$ cells overexpressing wild-type TUBB-V5 after 24 h serum withdrawal. Cells were immunostained for V5 and the ciliary marker ARL13B, and the percentage of cells showing ARL13B-positive cilium was measured in the transfected (V5-positive) and non-transfected (V5-negative) cell populations. Data from three experiments (n = 200 cells for V5-positive and n = 200 cells for V5-negative populations per experiment) are represented as mean ± standard deviation. P-value was calculated using an unpaired two-tailed t-test. (b) Ciliation frequency of cells overexpressing wild-type or mutant (P287L, E108K, L150F, T178S, K216R, L228V, E410D, N89T, R282Q, G437S) TUBB-V5 after 24 h serum withdrawal. Percentage of cells showing ARL13B-positive cilium was measured in the transfected (V5-positive) and non-transfected (V5-negative) cell populations (n = 200 cells for V5-positive population and n = 400 cells for V5-negative population per technical replicate). For each mutation, clinical significance from the ClinVar database is shown. The graph presents pooled data from single-replicate preliminary experiments on TUBB variants with undetermined clinical significance at the time of this study. For the wild-type control sample, data from five experiments are represented as mean ± standard

deviation. (c) Representative images of hTERT-RPE1 cells overexpressing wild-type or mutant (G308S) TUBB-V5 from the experiment in Figure 10. Cells were fixed after 24 h serum withdrawal and immunostained for V5 (green) and the ciliary marker ARL13B (not shown). Examples of complete microtubule incorporation, partial microtubule incorporation, and diffuse distribution of TUBB-V5 are shown. (d) Percentage of V5-positive cells from the experiment in Figure 10 showing complete microtubule incorporation, partial microtubule incorporation, and diffuse distribution of TUBB-V5 as determined by the appearance of the V5-signal. Pooled data from at least three experiments (n = 200 cells per technical replicate) are represented as mean ± standard deviation.

Source data are provided as a Source Data file.

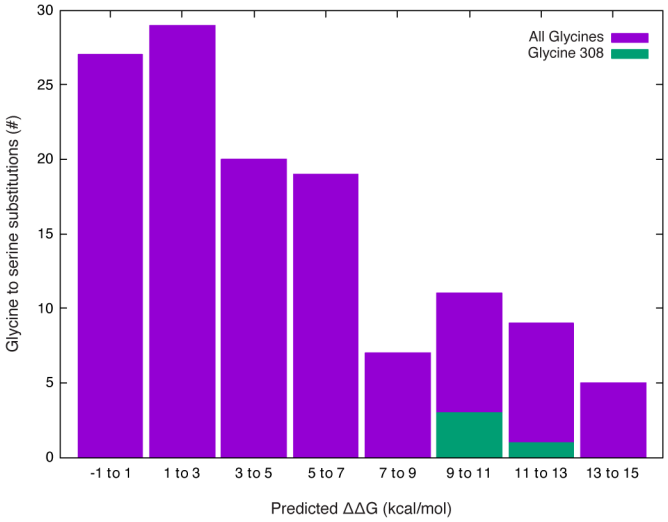


Figure S12. The G308S mutation is predicted to destabilize TUBB fold. *In silico* protein stability analysis on 4 beta-tubulin structures from 3 species (Protein Data Bank identifiers [PDB IDs]: 4i4t, 5nqu, 5yl2, 5ca1). The effect of every possible glycine to serine substitution was evaluated (software: FoldX). Combined results are shown.

$\Delta\Delta G = \Delta G_{\text{mutant}}\ (\text{folding}) - \Delta G_{\text{wild-type}}\ (\text{folding}); \quad \Delta\Delta G > 0$ if the mutation is destabilizing

Source data are provided as a Source Data file.

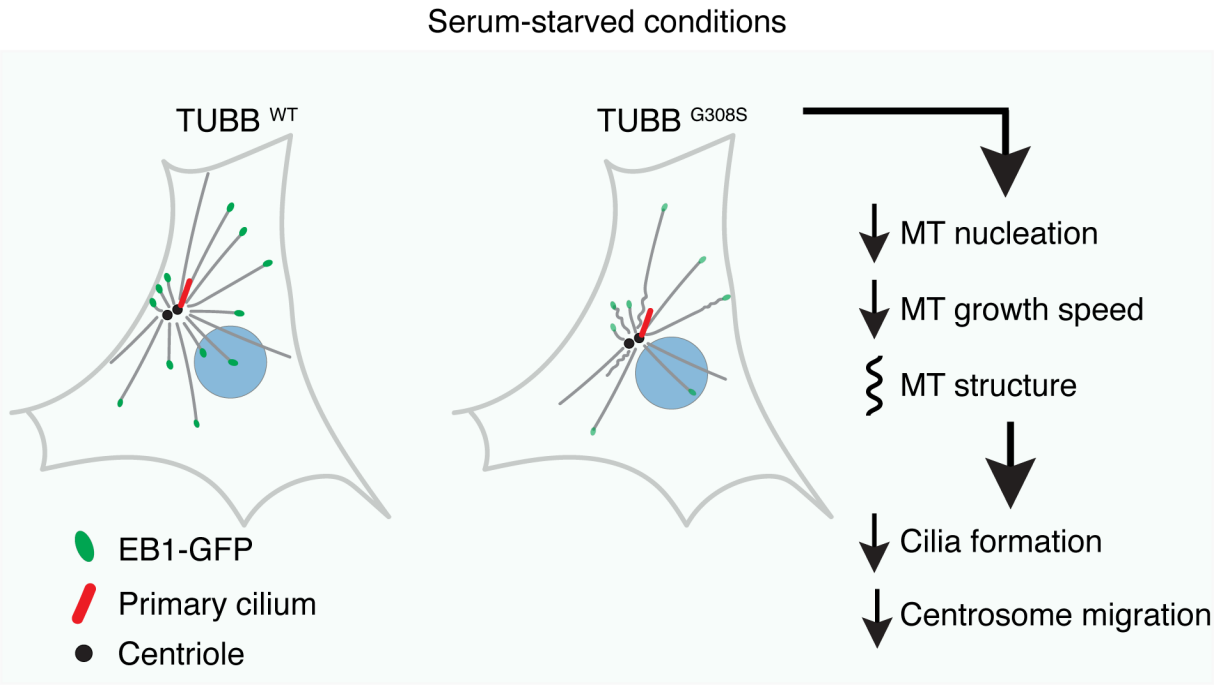


Figure S13. Possible model for the effects of TUBB G308S on ciliogenesis. In serum-starved TUBB^{G308S} hTERT-RPE1 cells, the reduced nucleation, altered (wavy and buckled) structure, and decreased growth speed of MTs (grey) lead to impaired primary cilia formation and centrosome migration during ciliogenesis.

Primary cilia formation depends on the dynein-mediated transport of pre-ciliary vesicles (PCVs) to the mother centriole in the early stages of ciliogenesis[31,33]. The reduced MT density and the structural abnormalities of the existing MTs likely affect PCVs transport, as variations in MT structure such as bending and buckling have been shown to contribute to motor-mediated MT transport and influence vesicle motion[66]. Moreover, we observe that dynein-mediated vesicular trafficking is disrupted in serum-starved TUBB^{G308S} cells. Dynein recruitment to MT plus-end may be impaired in TUBB^{G308S} cells. It depends on the previous recruitment of EB1 (green)[63], which we observe to be significantly reduced in TUBB^{G308S} (lighter green) compared to TUBB^{WT} cells (darker green). Importantly, EB1 recruitment has been shown to be affected by alterations in MT structure[64,65].

Migration of the ciliated centrosome to the plasma membrane occurs at a later stage of ciliogenesis and it is driven by pushing forces from MTs nucleation, bundling and polymerization[35]. Consistent with this, the impaired nucleation, altered structure and decreased growth speed of MTs affect this movement in TUBB^{G308S} cells.